

Giant anisotropic photocurrent modulated by strain in type-II Weyl semimetal T_d -MoTe₂

Xinru Wang¹, Ying Ding¹, M. N. Chen¹, Z. B. Siu², Mansoor B. A. Jalil^{2,*} and Yuan Li^{1,†}

¹ *Department of Physics, Hangzhou Dianzi University, Hangzhou, Zhejiang 310018, China and*

² *Computational Nanoelectronics and Nano-device Laboratory,*

Electrical and Computer Engineering Department, National University of Singapore,

4 Engineering Drive 3, Singapore 117576, Singapore

(Dated: November 23, 2021)

We build a Cu-MoTe₂-Cu device model and use first-principles density functional theory to study the transport properties of single-layer T_d -MoTe₂. We obtained the effect of strain on the energy band structure, transport properties, and photocurrent. The strain-induced photocurrent shows an anisotropy that reflects the modulation of the energy bands, including the Weyl point, by strain. The photocurrent can be suppressed to almost zero when the strain is applied along the vacuum direction. In contrast, the photocurrent can be significantly increased when the strain is applied along the transport direction. The transport properties and magnitude of the photocurrent in the MoTe₂-based device can be effectively modulated by adjusting the strength and direction of the strain.

PACS numbers: 78.67 -n, 73.63.-b

I. INTRODUCTION

The continuous in-depth research on the theory and fabrication technology of two-dimensional material devices in recent years has witnessed a development from the initial silicon materials to graphene-based layered nanomaterials [1, 2], and subsequently to the current transition metal chalcogenide materials. Two-dimensional transition-metal dichalcogenides (TMDs) [3] have quickly become a research hotspot in the field of materials because of their high carrier mobility, appropriate band gap, large switching ratio, and layer-dependent band gap [4–6]. MoTe₂ is an important part of the TMD family. MoTe₂ exists in three phases [7], namely, the hexagonal (2H, semiconductor), monoclinic (1T', metal), and octahedral (T_d , type-II Weyl semimetal) phases. Our main research subject is T_d -MoTe₂, which has been theorized to be an example of a Type-II Weyl semimetal [8–10].

The Type-II Weyl semimetal is a generalization of the Weyl semimetal. Its defining characteristic is the inclination of the Dirac cone near the Weyl point, which results in a corresponding electronic dispersion relation that does not satisfy Lorentz invariance near the Weyl point [11]. T_d -MoTe₂ has rich physical properties which include superconductivity [12], extremely large magnetoresistance (XMR) [13], and topological semi-metal properties. Because single-layer T_d -MoTe₂ is predicted to host the quantum spin Hall (QSH) insulating state, this material has attracted much attention in the study of condensed matter physics.

In this study, we calculate the transport properties of

two-dimensional MoTe₂-based devices based on quantum transport simulations in which density functional theory (DFT) is combined with the non-equilibrium Green's function (NEGF) [14–16] formalism. We analyze the effect of the strain on the energy band diagram, transmission spectrum, and photocurrent of layered T_d -MoTe₂ to provide a theoretical basis for subsequent experimental research.

II. THEORETICAL MODEL AND METHOD

We model a device with the Cu-MoTe₂-Cu configuration in which a T_d -MoTe₂ central region is sandwiched between two copper leads. Fig. 1(a) shows the unit cell of T_d -MoTe₂. The space group of T_d -MoTe₂

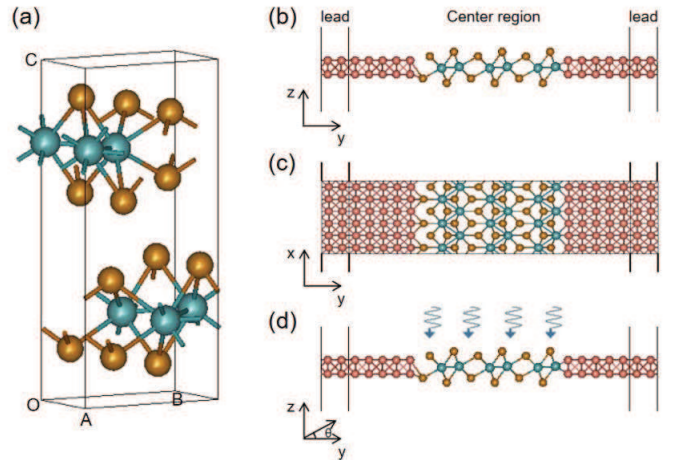


FIG. 1: (a) The unit cell of T_d -MoTe₂. (b) Side and (c) top view of Cu-MoTe₂-Cu transport model. (d) The T_d -MoTe₂ in the central region is irradiated by linearly polarized light.

*Electronic address: elemhaj@nus.edu.sg

†Electronic address: liyuan@hdu.edu.cn

is $\text{Pmn}2_1(\text{No.}31)$ and the lattice parameters are $a = 3.477\text{\AA}$, $b = 6.335\text{\AA}$, and $c = 13.889\text{\AA}$. These datum are consistent with previously reported structure [12]. The device model is shown in Fig. 1(b) and (c). The y direction is the transport direction, and the x direction is the transverse periodic direction which extends to $\pm\infty$ so that the device lies on the $x - y$ plane. The z axis is the vacuum direction. A 40\AA vacuum region is used to separate the devices in this direction. As shown in Fig. 1(d), strain and linearly polarized light are applied to the $\text{T}_d\text{-MoTe}_2$ in the central region.

The DFT-based software package Nanodcal [17] was used for transport calculations in this study. In the quantum transport calculations, the charge density was obtained through self-consistent calculations and the conductivity in turn calculated from the charge density. The LDA_PZ81 generalized gradient approximation was

used in the DFT calculations to describe the exchange-correlation energy. The plane wave basis set cutoff energy was set as 100 Hartrees (1 Hartree = 27.21 eV). The Brillouin zone of $\text{T}_d\text{-MoTe}_2$ was sampled with a $10 \times 11 \times 1$ k-mesh for geometry optimization and the self-consistent calculations. The self-consistent threshold for the total energy of the system was 10^{-4} eV and the strain of the system converged to 0.04 eV/A in the relaxation calculation.

The strain is applied to the $\text{T}_d\text{-MoTe}_2$ material in the central region. The wavy lines in Fig. 1(d) schematically represent the illumination of linearly polarized light. The polarized light is incident on the $x - y$ plane and polarized at an angle θ with respect to the transport direction. When the $\text{T}_d\text{-MoTe}_2$ central region is irradiated by linearly polarized light, a photocurrent is generated. The photocurrent can be written as [18–20]

$$J_L^{(ph)} = \frac{ie}{h} \int \left\{ \cos^2 \theta \text{Tr} \left\{ \Gamma_L \left[G_1^{<(ph)} + f_L \left(G_1^{>(ph)} - G_1^{<(ph)} \right) \right] \right\} + \sin^2 \theta \text{Tr} \left\{ \Gamma_L \left[G_2^{<(ph)} + f_L \left(G_2^{>(ph)} - G_2^{<(ph)} \right) \right] \right\} \right. \\ \left. + 2 \sin(2\theta) \text{Tr} \left\{ \Gamma_L \left[G_3^{<(ph)} + f_L \left(G_3^{>(ph)} - G_3^{<(ph)} \right) \right] \right\} \right\} dE, \quad (1)$$

where

$$G_1^{>(<)ph} = \sum_{\alpha, \beta=x, y, z} C_0 N G_0^r e_{1\alpha} p_\alpha^\dagger G_0^{>(<)} e_{1\beta} p_\beta G_0^a, \\ G_2^{>(<)ph} = \sum_{\alpha, \beta=x, y, z} C_0 N G_0^r e_{2\alpha} p_\alpha^\dagger G_0^{>(<)} e_{2\beta} p_\beta G_0^a, \\ G_3^{>(<)ph} = \sum_{\alpha, \beta=x, y, z} C_0 N G_0^r (e_{1\alpha} p_\alpha^\dagger G_0^{>(<)} e_{2\beta} p_\beta + e_{2\alpha} p_\alpha^\dagger G_0^{>(<)} e_{1\beta} p_\beta) G_0^a. \quad (2)$$

Here $G_{1,2,3}^{>(<)ph}$ is the greater or lesser Green's function of the electron-photon interaction, which is dependent on the photon frequency ω , and f_L is the Fermi-Dirac distribution function. $C_0 = \frac{e^2 \hbar \sqrt{\mu_r \epsilon_r}}{2N m^2 \omega \epsilon c} I_\omega$ where m is the bare electron mass, the photon flux I_ω is the number of photons per unit area per unit time, N is the number of photons, ϵ is the dielectric constant, and ϵ_r is the relative dielectric constant. In our calculations, the polarization vector $\hat{e} = \cos\theta \hat{e}_1 + \sin\theta \hat{e}_2$ describes the polarization of the incident light. The unit vectors \hat{e}_1 and \hat{e}_2 are set along the y and x directions, respectively. The photocurrent can be normalized as $J = J_L^{(ph)}/eI_\omega$.

All the calculations were performed using the quantum transport package in Nanodcal, which is based on DFT. The atomic cores were defined using non-local pseudopotentials and the interactions between the $\text{T}_d\text{-MoTe}_2$ centre region and the copper leads of the device calculated

using NEGF. By combining DFT and NEGF, the calculation time for NEGF is shortened, and the accuracy of the DFT calculation results is improved. The obtained band structure of MoTe_2 along several high-symmetry lines in the Brillouin zone are shown in Fig. 2. According to the results of Soluyanov et al. [11], the Type-II Weyl node results in a non-closed contact between the conduction band (CB) and valence band (VB) and an open Fermi surface. As shown in Fig. 2(a) (see inset), there is a Weyl point between the high-symmetry points G and X, which is consistent with the characteristics of the Type-II Weyl semimetal. In addition, a band crossing region can be observed along the path S-G. There exist three distinct values of energy separation, viz. 0.98, 2.28, and 1.78 eV, between the local energy extrema of the CB and VB. The following calculation results show that strain can break the energy crossings at the Weyl points in $\text{T}_d\text{-MoTe}_2$.

III. RESULTS AND DISCUSSION

The strain is first applied to $\text{T}_d\text{-MoTe}_2$ along the y direction (transport direction). The strength of the strain is expressed as $\zeta = (b - b_0)/b_0$ where b_0 and b are the lattice constants of the model in the absence and presence of the strain, respectively. The maximum value of the strain used in the calculations was $\zeta = 10\%$ to maintain a realistic structure for $\text{T}_d\text{-MoTe}_2$. Figs. 2(b)-(d) show the energy bands obtained when 3%, 6% and 9% strain

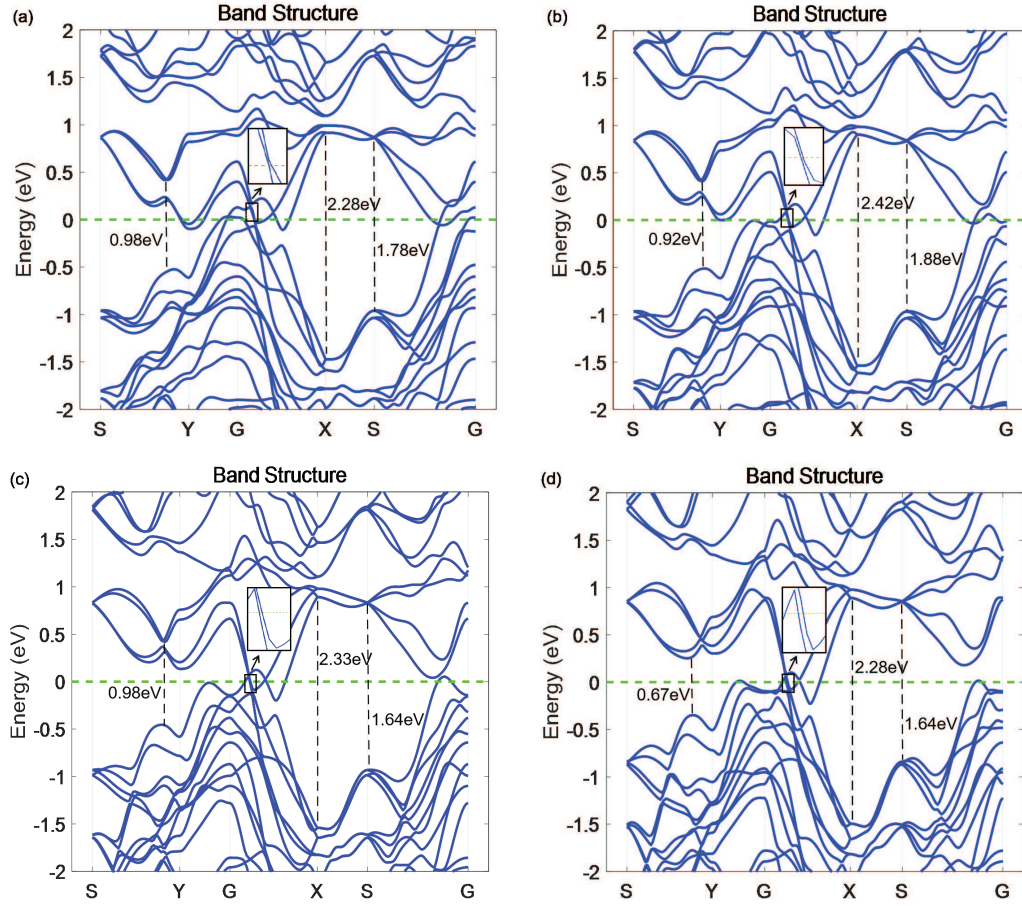


FIG. 2: Energy band structure of Td-MoTe₂ for different strain strengths exerted along the x direction: (a) $\varepsilon = 0$, (b) $\varepsilon = 3\%$, (c) $\varepsilon = 6\%$, and (d) $\varepsilon = 9\%$.

are applied along the transport direction. At 3% strain, the bands that form the Weyl point begin to separate because of the strain although the energy bands have no distinct change. The energy level spacings are correspondingly changed. For example, the left level spacing decreases from 0.98 eV to 0.92 eV. When the strain increases to 6%, the bands forming the Weyl point further separate and the crossing of the energy bands along the path S-G is also broken by the effect of the strain. With the strain increases to 9%, the Weyl point is completely broken and a large energy separation appears between the original crossing energy bands. The left and right energy level spacings are significantly decreased to about 0.67 eV and 1.64 eV, respectively.

To investigate the effect of strain on the transport property, we study the transmission of electrons in the Cu-MoTe₂-Cu device under the action of the strain applied along the y direction. Fig. 3 shows the variation of the transmission with the strength of the strain. When $\zeta = 0$, there exist three transmission peaks near $E = -1.3$, -0.5 , and 0.9 eV. This implies that there are more quantum states that contribute to the transmission near the three energies. When the strain is increased to

$\zeta = 3\%$ and 6% , the peak value of the transmission at $E = 0.9$ eV is significantly decreased to about 1. In particular, the transmission decreases to about 0.1 within the energy interval of $0 < E < 0.15$ eV at $\zeta = 6\%$, which is associated with the breaking of the energy band crossing along the S-G path shown in Fig. 2(c). When the strain increases further to 9%, the Weyl point is completely broken. Correspondingly, the transmission peak in the energy interval $0 < E < 0.25$ eV drops to a small value because of the strain. In addition, the sharp transmission peak near $E = 0.9$ eV evolves to a broad transmission peak, which is attributed to the accumulation of quantum states within the energy interval of $0.5 < E < 1$ eV observed in Fig. 2(d). The transmission curves can reflect the effect of strain on the energy bands obviously, including the variation of the Weyl points.

We next analyze the photocurrent of the Cu-MoTe₂-Cu under varying strains along the y axis to study the effect of strain on the transport characteristics of the MoTe₂ systems. Because single-layer Td-MoTe₂ has no spatial inversion symmetry, the vertical irradiation of linearly polarized light can induce a large photogalvanic effect (PGE) and thereby generate photocurrent. We calculate

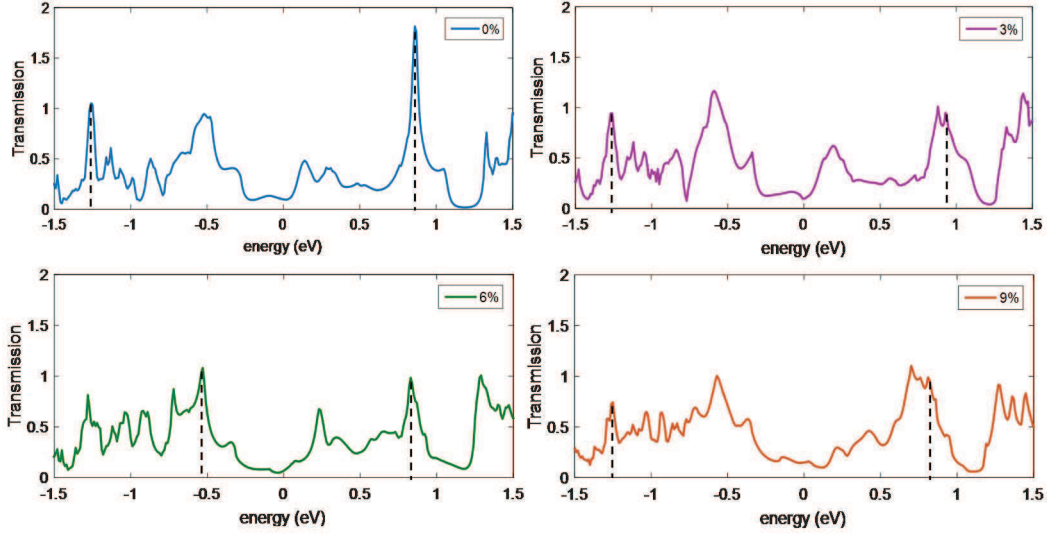


FIG. 3: The electron transmission plotted as a function of the Fermi energy for different amplitudes of the strain applied along y axis.

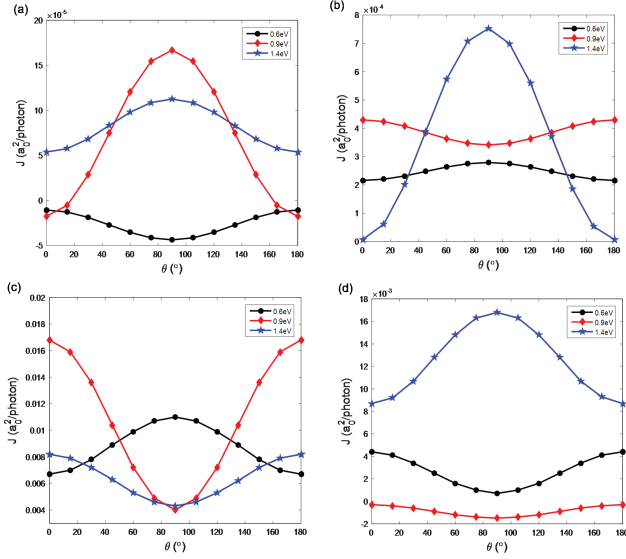


FIG. 4: The photocurrent generated in the Cu-MoTe₂-Cu is plotted as a function of the polarization angle of the linearly polarized light θ for photon energies from 0.6 eV to 1.4 eV. The strain is applied along the x direction with the amplitudes of (a) $\zeta = 0$, (b) $\zeta = 3\%$, (c) $\zeta = 6\%$ and (d) $\zeta = 9\%$.

the photocurrent for photon energies from 0.1 eV to 2.4 eV, which covers the near-infrared and visible light range. As shown in Fig. 4, we find that for all the photon energies considered, there is a $\cos(2\theta)$ relationship between the polarization angle θ and the photocurrent. Our calculated results for the photocurrent under C_s symmetry are therefore consistent with the phenomenological theory of PGE [21–23]. When $\zeta = 0$, the photocurrent has a relatively large value of about 1.7×10^{-4} at $\theta = 90^\circ$ and the photon energy 0.9 eV. All three curves exhibit the

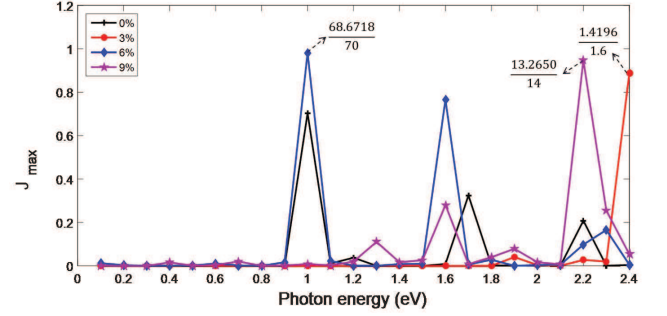


FIG. 5: The maximum photocurrent in the Cu-MoTe₂-Cu induced by linearly polarized light for photon energies from 0.1 eV to 2.4 eV under strains of $\zeta = 0, 3\%, 6\%$, and 9% applied along the y direction. To clearly show the variation of the photocurrent, the three peak values are scaled by a multiple. For example, $68.6718/70$ means that the peak value is scaled to one seventieth of its actual value.

$\cos(2\theta)$ dependence. As the strain increases, the maximum value of the photocurrent increases to 0.0168 at the strain strengths of $\zeta = 6\%$ and 9% , as shown in Figs. 4(c)-(d). We therefore find that for any given photon energy, the maximum values of the photocurrent are obtained at either $\theta = 0^\circ$ or $\theta = 90^\circ$. When strain is applied to T_d-MoTe₂ along these two directions, the cosine-curve relationship is preserved because the strain does not change the symmetry of T_d-MoTe₂. For further study, we consider the maximum value of the photocurrent J_{max} at different photon energies to analyze the effect of the strain on the photocurrent.

In Fig. 5, the maximum photocurrent J_{max} is plotted as a function of the photon energy for different strengths of the strain. There are three peaks in J_{max} in the absence of the strain. The peak values of J_{max} are about

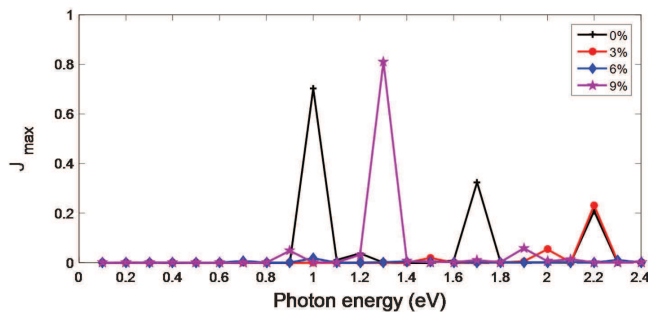


FIG. 6: The maximum photocurrent in the Cu-MoTe₂-Cu induced by linearly polarized light for photon energies from 0.1 eV to 2.4 eV under strains of $\zeta = 0\%$, 3% , 6% , and 9% applied along the z direction.

0.7, 0.35, and 0.2 at the respective photon energies of 1 eV, 1.7 eV, and 2.2 eV. These three peaks arise from the transition of electrons from the VB to the CB, which are associated with the three energy spacings of 0.98, 1.68, and 2.28 eV, as shown in Fig. 2. When $\zeta = 3\%$, the largest photocurrent occurs at the photon energy of 2.4 eV and increases to 1.4196. Interestingly, when the strain is increased to $\zeta = 6\%$, the photocurrent increases significantly to 68.6718 at the photon energy of 1 eV, which is about 92 times the photocurrent at $\zeta = 0$. The shift of the photon energy at which the three peak photocurrent values occur to 1 eV, 1.6 eV and 2.3 eV reflects the change in the three energy spacings in Fig. 2(c). Especially, when the energy spacing is 1 eV, the energy extremas of two CBs close to each other and more quantum states can contribute to the large photocurrent. When $\zeta = 9\%$, the photocurrent has four peaks, among which the largest value of 13.265 occurs at 2.2 eV. The above results show that strain can be utilized to significantly enhance the photocurrent, and that the photocurrent can reflect the detailed changes in the band structure, including the modification of the Weyl point induced by the strain.

We further study the anisotropy of the strain-induced photocurrent by considering the application of strain along the z direction. Fig. 6 shows the corresponding J_{max} induced by linearly polarized light with photon energies from 0.1 eV to 2.4 eV when the strain is applied along the z direction. When $\zeta = 3\%$, there exist two photocurrent peaks at the photon energies of 2 eV and 2.2 eV. The peak value of J_{max} at 2 eV is about 0.05. With the increase of the strain to $\zeta = 6\%$, the photocur-

rent significantly decreases to zero. When $\zeta = 9\%$, two peaks occur at 1.3 eV and 1.9 eV. The peak value of J_{max} at 1.3 eV increases to about 0.82, which is close to the value of the photocurrent when $\zeta = 0$. The peak values of the photocurrent tends to be lower than that observed under strain which is applied in the y or transport direction. The above results show that the strain-induced photocurrent exhibits a large anisotropy to the strain direction: The photocurrent can be suppressed to almost zero when the strain is exerted along the z direction. In contrast, the photocurrent can be significantly increased to 92 times that of the photocurrent at $\zeta = 0$ when the strain is exerted along the y or transport direction. This suggests that an effective modulation of the photocurrent can thus be realized by utilizing strain.

IV. CONCLUSIONS

In conclusion, we have studied the effect of strain on the energy band structure of T_d-MoTe₂ and the transport properties and photocurrent in a MoTe₂-based device. Density functional theory was used to calculate the energy band structure and electron transmission spectrum of T_d-MoTe₂ under different strains. The results show that strain can effectively modulate the energy bands and result in the destruction of Weyl points. The transmission peaks reflect the variation of the energy bands induced by the strain. The strain-induced photocurrent shows an anisotropic dependence on the direction of the strain which reflects the variation of the energy bands, including the Weyl point, modulated by the strain. The photocurrent can be suppressed to almost zero when the strain is exerted along the z direction. In contrast, the photocurrent can be significantly increased to 92 times that of the photocurrent at $\zeta = 0$ when the strain is applied along the y direction. An effective modulation of the photocurrent can thus be realized by utilizing strain. These findings on the strain-modulated transmission and photocurrent are valuable for the exploration of novel MoTe₂-based devices, especially optoelectronic devices.

This work was supported by National Natural Science Foundation of China (Grant No. 11574067).

Conflict of interest The authors have no conflicts to disclose.

DATA AVAILABILITY The data that support the findings of this study are available from the corresponding author upon reasonable request.

[1] B Govinda Rao, Hssr Matte and Cnr Rao, *Journal of Cluster Science* **23**, 929-937 (2012).
 [2] B. Mondal, K. Sengupta, A. Rana, A. Mahammed and A. Dey, *Inorganic Chemistry* **52**, 3381-3387 (2013).
 [3] J. A. Wilson and A. D. Yoffe, *Advances in Physics* **18**, 193-335 (1969).

[4] Z. Xin, Q. H. Tan, J. B. Wu, S. Wei and P. H. Tan, *Nanoscale* **8**, 6435-6450 (2016).
 [5] J. Luxa, O. Jankovsky and D. Sedmidubsky, *Nanoscale* **8** 1960-1967 (2015).
 [6] H. Zeng and X. Cui, *Chemical Society Reviews* **44**, 2629-2642 (2015).

- [7] W. G. Dawson and D. W. Bullett, *Journal of Physics C Solid State Physics* **20**, 6159 (1987).
- [8] Z. Guguchia, F. Von Rohr, Z. Shermadini, A. T. Lee, S. Banerjee, A. R. Wieteska, C. A. Marianetti, Frandsen BA, H. Luetkens and Z. Gong, *Nature Communications* **8**, 1082 (2017).
- [9] J. Jiang, Z. K. Liu, Y. Sun, H. F. Yang, C. R. Rajamathi, Y. P. Qi, L. X. Yang, C. Chen, H. Peng and C. C. Hwang, *Nature Communications* **8**, 13973 (2017).
- [10] K. Deng, G. Wan, P. Deng, K. Zhang, S. Ding, E. Wang, M. Yan, H. Huang, H. Zhang and Z. Xu, *Nature Physics* **12**, 1105-1110 (2016).
- [11] A. A. Soluyanov, D. Gresch, Z. Wang, Q. S. Wu, M. Troyer, D. Xi and B. A. Bernevig, *Nature* **527**, 495-498 (2015).
- [12] Y. Qi, P. G. Naumov, M. N. Ali, C. R. Rajamathi, W. Schnelle, O. Barkalov, M. Hanfland, S. C. Wu, C. Shekhar and Y. Sun, *Nature Communications* **7**, 11038 (2016).
- [13] H. K. Dong, S. Cho, J. H. Kim, D. H. Choe and Y. H. Lee, *Nature Physics* **11**, 482-486 (2015).
- [14] A. P. Jauho, N. S. Wingreen and Y. Meir, *Physical Review B* **50**, 5528 (1994).
- [15] B. G. Wang, J. Wang and Hong Guo, *Physical Review Letters* **82**, 398 (1999).
- [16] B. G. Wang, J. Wang and Hong Guo, *Journal of Applied Physics* **86**, 5094 (1999).
- [17] Jeremy Taylor, Hong Guo and Jian Wang, *Physical Review B* **63**, 245407 (2001).
- [18] Y. Q. Xie, L. Zhang, Y. Zhu, L. Liu and H. Guo, *Nanotechnology* **26**, 455202 (2015).
- [19] M. M. R. Moayed, F. Li, P. Beck, J. C. Schober and K. K., *Nanoscale* **12**, 6256 (2020).
- [20] Y. Luo, Y. Hub and Y. Xie, *Journal of Materials Chemistry A* **7**, 27503 (2019).
- [21] V. I. Belinicher, B. I. Sturman, *Soviet physics Uspekhi* **23**, 451-458 (1980).
- [22] J. Hu, W. Xiong, C. Z. Cai, J. W. Wang, J. J. Li, Y. Q. Xie, Y. Wang, *Applied Physics Letters* **115**, 151104 (2019).
- [23] Y. Q. Xie, M. Y. Chen, Z. W. Wu, Y. B. Hu, Y. Wang, J. Wang, H. Guo, *Physical Review Applied* **10**, 034005 (2018).